ChemistryOpen

Research Article
doi.org/10.1002/open.202100250

Chemistry Europe
European Chemical Societies Publishing

www.chemistryopen.org

Computational Study of Mechanism and Enantioselectivity of Imine Reductase from *Amycolatopsis orientalis*

Mario Prejanò,[a] Xiang Sheng,[b] and Fahmi Himo*[a]

Imine reductases (IREDs) are NADPH-dependent enzymes (NADPH = nicotinamide adenine dinucleotide phosphate) that catalyze the reduction of imines to amines. They exhibit high enantioselectivity for a broad range of substrates, making them of interest for biocatalytic applications. In this work, we have employed density functional theory (DFT) calculations to elucidate the reaction mechanism and the origins of enantioselectivity of IRED from *Amycolatopsis orientalis*. Two substrates are considered, namely 1-methyl-3,4-dihydroisoquinoline and 2-propyl-piperideine. A model of the active site is built on the basis of the available crystal structure. For both substrates, different binding modes are first evaluated, followed by calculation of the hydride transfer transition states from each complex. We have also investigated the effect of mutations of certain important active site residues (Tyr179Ala and Asn241Ala) on the enantioselectivity. The calculated energies are consistent with the experimental observations and the analysis of transition states geometries provides insights into the origins of enantioselectivity of this enzyme.

Introduction

Imine reductases (IREDs) catalyze the reduction of imines to amines using nicotinamide adenine dinucleotide phosphate (NADPH) as a cofactor (Scheme 1).[1–5] The reaction can afford primary, secondary and tertiary amines, and these enzymes have received increasing attention in recent years due to their potential applications as catalysts for the synthesis of chiral amines. Enzymatic reduction of imines provides an economic and eco-friendly alternative strategy to metal-assisted catalytic routes.[6] IREDs are also used in enzymatic cascade reactions, working in tandem with lipases, carboxylic acid reductases, transaminases and ketoreductases.[1–3,7–9]

The IRED from *Amycolatopsis orientalis* (*Ao*IRED), the focus of the current computational study, has been characterized in terms of its catalytic and structural properties.[10] The enzyme exhibits high enantioselectivity for a broad range of substrates.[10] Similarly to other IREDs,[11] the catalytic site of *Ao*IRED encompasses two pockets in which the substrate and the cofactor bind, respectively.[10] The crystal structure was obtained in the *apo* form (PDB 5A9R), in complex with NADP (PDB 5A9S), and with NADPH and (*R*)-1-methyl-1,2,3,4-tetrahydroisoquinoline, ***R*-2** (Figure 1, PDB 5FWN).[10] It has been suggested that the activity of *Ao*IRED is related to conformational changes that take place in proximity of the active site upon the binding of cofactor and substrate.[10] This hypothesis is based on the structural comparison of the binary complex IRED:NADPH and the *apo* form of IRED, which are characterized by "closed" and "open" conformations, respectively.[10]

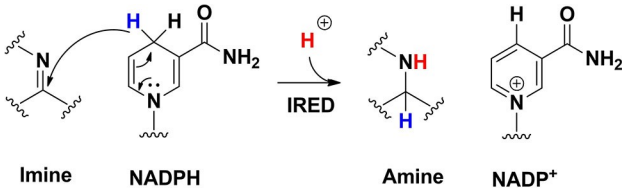

Scheme 1. Reaction catalyzed by imine reductases.

The crystal structure of the ternary complex IRED:NADPH:***R*-2** sheds light on the active site residues that could be involved in controlling the stereoselectivity. Site-directed mutagenesis demonstrated the involvement of Tyr179 and Asn241 in the stereocontrol, and for bulky substrates, the mutation of each of these two residues resulted in the inversion of enantioselectivity.[10]

Detailed understanding of the reaction mechanism and the origins of the stereocontrol for different substrates is of importance for the further utilization of IREDs in biocatalysis, as it can be used to design new variants with tailored reactivities and selectivities.[12] To this end, we herein report a computational investigation of the reaction mechanism of *Ao*IRED, adopting the quantum chemical cluster approach. In recent years, this methodology has been applied to study the

[a] *Dr. M. Prejanò, Prof. Dr. F. Himo*
Department of Organic Chemistry
Arrhenius Laboratory, Stockholm University
10691 Stockholm (Sweden)
E-mail: fahmi.himo@su.se
[b] *Prof. Dr. X. Sheng*
Tianjin Institute of Industrial Biotechnology
Chinese Academy of Sciences and National Technology Innovation Center of Synthetic Biology
Tianjin 300308 (China)

Supporting information for this article is available on the WWW under https://doi.org/10.1002/open.202100250

This publication is part of a joint Special Collection with ChemCatChem on "BioTrans 2021". Please see our homepage for more articles in the collection.

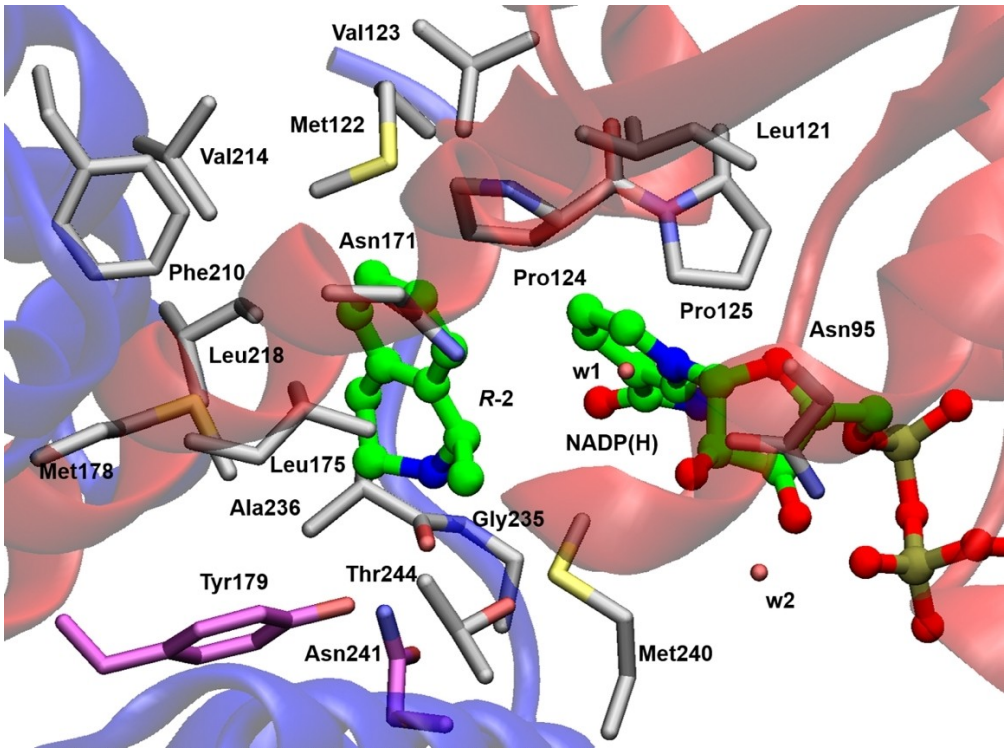

Figure 1. Active site of *Ao*IRED (PDB 5FWN)[10] in complex with NADPH and (*R*)-1-methyl-1,2,3,4-tetrahydroisoquinoline (**R-2**). Carbon atoms of Tyr179 and Asn241 residues are highlighted in violet.

mechanisms and origins of enantioselectivity of a number enzymes used in asymmetric biocatalysis.[13,14]

We focus on two different substrates, 1-methyl-3,4-dihydroisoquinoline (**1**) and 2-propyl-piperideine (**3**). In the case of **3**, the *R*-product (***R*-4**) is favored (Scheme 2), while in the case of **1**, the stereochemical outcome is quite intriguing, as the stereochemistry for this substrate changes during the storage of *Ao*IRED. Using fresh lysate and freshly purified enzyme result in the formation of the *S*-product, while, after storage, it yields the *R*-product.[10] No clear explanation is currently available for this phenomenon. As will be discussed below, the results of the current calculations agree very well with the observations for the freshly purified enzyme. To gain further insight, we have also considered the effects of the Tyr179Ala and Asn241Ala mutations on the selectivity of substrate **1**.

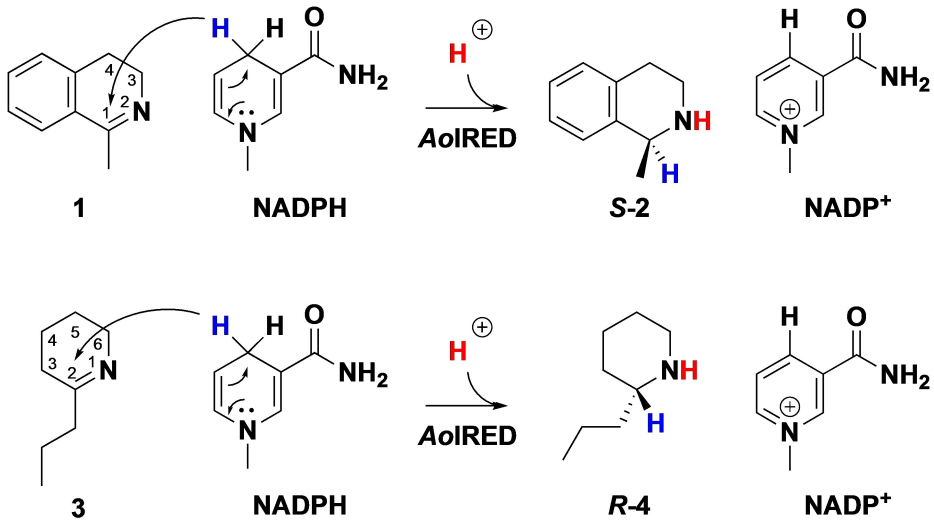

Scheme 2. Reactions investigated in the present work.

Computational Methods

Technical Details

All calculations were performed using the B3LYP-D3(BJ) functional as implemented in Gaussian16 C.01 program.[15,16] The geometry optimizations were carried out employing the 6-31G (d,p) basis set. At the same level of theory, the effects of surrounding were estimated using single-point SMD solvation calculations, with $\varepsilon = 4$.[17] Frequencies were also calculated to obtain zero-point energy (ZPE) corrections. Finally, single-point energy calculations were performed using the much larger 6-311+G(2d,2p) basis set to obtain more accurate electronic energies. The final energies presented in the paper are thus the large basis set ones, corrected for ZPE and solvation.

Active Site Model

An active site model was designed on the basis of the crystal structure of *Ao*IRED in which the NADPH and the (*R*)-1-methyl-1,2,3,4-tetrahydroisoquinoline ***R*-2** are bound in the active site (PDB 5FWN).[10] ***R*-2** was manually replaced by substrates **1** or **3**. Apart from the substrate and the NADPH cofactor, the model consists of the amino acids that make up the cofactor-binding site (Met16, Asn95, Ile121, Val123, Pro124, Pro125, Asn171 and Met178) and the substrate-binding site (Met122, Leu175, Tyr179, Phe210, Val214, Ile218, Ala235, Gly236, Met240, Asn241 and Thr244), as shown in Figure 2. In addition, two crystallographic water molecules (w1 and w2) that are present in the crystal structure and that interact with the cofactor and Asn95 were also explicitly included in the model.

The NADPH cofactor and the various amino acids were truncated as shown in Figure 2, and hydrogen atoms were added manually to saturate the carbon atoms. The carbon atom where the truncation was made, and one of its hydrogens, were kept fixed during geometry optimizations (fixed centers are labeled with an asterisk in the figures below).

This procedure is a necessary element of the cluster approach in order to avoid large, unrealistic movements of the various groups of the active site model. When the model is sufficiently large, like the case of the current model of *Ao*IRED, the active site residues have, despite being anchored by the fixed atoms, enough flexibility to adapt to changes in the geometries of the reacting parts during the reaction. However, when modeling enzymatic enantioselectivity, one has to reproduce quite small energy differences between transition states. Therefore, even small errors due to the size of the model and the atom fixing procedure can lead to over- or underestimation of the selectivity.[13,14]

At the pH of the experiments, the imine substrates are expected to be in the protonated form, and substrates **1** and **3** were therefore modeled as iminium ions in the calculations.[10] The final size of the model is 322 and 324 atoms for substrates **1** and **3**, respectively, and the total charge is +1.

Results and Discussion

For each of the two studied substrates, the geometries of a number of enzyme-substrate (ES) complexes were optimized to

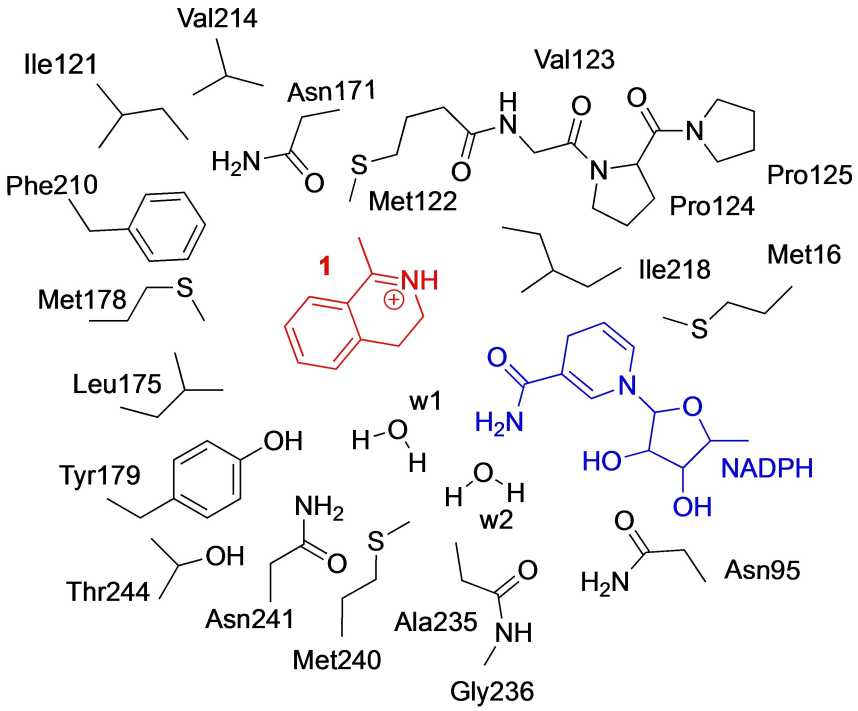

Figure 2. Schematic illustration of the active site model used in the current study, here with 1-methyl-3,4-dihydroisoquinoline (in the protonated form) as the substrate.

ensure that the lowest-energy binding modes are identified. The reaction mechanism was then followed for all considered ES complexes. Depending on how the C=N double bond of the imine moiety faces the hydride of the NADPH cofactor, the binding modes can lead to either *S*- or *R*-products. In the route to the *S*-product (*S*-path), the NADPH is located at the *Re* face, while in the *R*-path it is located at the *Si* face. The binding modes and the following transition states (TSs) will therefore have an *-S* or an *-R* in their names in the discussion below.

Reaction of 1-Methyl-3,4-dihydroisoquinoline

In the case of substrate **1**, eight ES complexes with different substrate orientations in the active site were optimized. The lowest-energy structures for the complexes leading to *S*- and *R*-products (called **E:1-*S*** and **E:1-*R***, respectively) are shown in Figure 3, while the other structures with higher energies are depicted in the Supporting Information. In **E:1-*S***, the imino group of **1** forms a hydrogen bond with the backbone of Met122, while in **E:1-*R***, it interacts with one of the water molecules in the active site (w1). In both cases, the overall conformations of the active site residues quite closely resemble the crystal structure, as can be seen from the superposition of the structures provided in the Supporting Information. Interestingly, despite the different orientations of the substrate, the two binding modes **E:1-*S*** and **E:1-*R*** have the same calculated energy. Other binding modes are up to 10 kcal mol^{-1} higher in energy, as shown in the Supporting Information.

The transition states of the hydride transfer step were then optimized for all ES complexes. The lowest-energy TS, called **TS-1-*S***, was found to lead to the *S*-product and stems from the lowest-energy binding mode **E:1-*S***. The calculated barrier for this is 20.1 kcal mol^{-1} (Figure 4), which is in good agreement with the measured k_{cat} of 0.74 s^{-1} that corresponds to a barrier of approximately 18 kcal mol^{-1}.[10] Importantly, the lowest-energy TS leading to the *R*-product (**TS-1-*R***) has a calculated barrier of 23.3 kcal mol^{-1}, that is, 3.2 kcal mol^{-1} higher than the *S*-path. This result is consistent with the stereopreference observed for the fresh lysate and fresh purified enzyme (85% and 81% ee, respectively, in favor of the *S*-enantiomer).[10]

Other optimized TSs are 4–7 kcal mol^{-1} higher than **TS-1-*S*** (see Supporting Information). The resulting enzyme-product complexes, **E:2-*S*** and **E:2-*R***, are calculated to be +11.9 kcal mol^{-1} and +7.9 kcal mol^{-1} relative to **E:1-*S***, respectively (structures are provided in the Supporting Information).

Scrutinizing the optimized geometries of **TS-1-*S*** and **TS-1-*R*** in Figure 3, as well as the other TSs in the Supporting Information, helps to shed light on the sources of the observed stereoinduction. We can identify a number of steric repulsions between the substrate and the surrounding groups in **TS-1-*R*** that are not present in **TS-1-*S***. The most relevant ones are the repulsions between the aromatic ring of the substrate and the side chains of Ile121 and Val214, and between the methylene group at the C4 position of the substrate and the amide group of the cofactor (Figure 3). In **TS-1-*S***, the substrate points in a different direction and these steric repulsions do not exist.

There are alternative TSs that lead to the *R*-product that lack these steric clashes, but they suffer from other features that cause their energies to be higher. For example, **TS1-1-*R2*** and **TS1-1-*R3*** (see Supporting Information) lack the H-bond between the imino moiety and the surrounding groups, and in **TS1-1-*R4*** the methyl substituent at the C1 position of the substrate clashes with Pro124.

In addition to the steric clashes, we also note that in **TS-1-*S*** the amide group of the cofactor has a favorable non-covalent attractive interaction with the aromatic ring of the substrate, while in **TS-1-*R***, this interaction is lacking. This is visible from a non-covalent interaction (NCI) plot[18] provided in the Supporting Information.

Taken together, these contributions result in a higher energy of **TS-1-*R*** relative to **TS-1-*S***, inducing thus the observed selectivity. It is interesting to note that the trend in energy between the *S*- and *R*-pathways in transition state is not the same as in the ES and EP complexes (Figure 4). In the ES complex, there is practically no difference in energy between the binding modes leading to the different products, while in the EP complex, the *R*-product binds better than the *S*-product. These observations mean that it is not possible to predict the stereochemical outcome by simply comparing the energies of the ES or EP complexes as commonly done in docking studies. The full energy profile, including the transition state energies, is required to make a qualified prediction.

To further analyze the stereoselectivity of *Ao*IRED toward substrate **1**, we have considered the effects of the Tyr179Ala and Asn241Ala mutations on the calculated energy barriers. Experimentally, an inversion from *S* to *R* was observed for both these mutants as compared to the freshly purified wild-type enzyme, with >98% ee for Tyr179Ala and 71% ee for Asn241Ala.[10]

We introduced these mutations to the active site model by replacing the side chains of the tyrosine or the asparagine residues by an ethyl group, representing the alpha and beta carbons of alanine. Such a protocol has been successfully applied in previous work addressing the effects of mutations on the enantioselectivity.[13a,j] For both mutants, we optimized a number of transition states for the hydride transfer, considering different binding modes and orientations of the substrate (in total 11 TSs for each mutation). The calculations could reproduce the experimental results, in that the energy of the TS for the *R*-pathway was found to be lower than the *S*-pathway for both the Tyr179Ala and Asn241Ala mutations, by 2.1 and 2.0 kcal mol^{-1}, respectively. By comparing the optimized TS structures of the *R*- and *S*-pathways with each other and with their wild-type counterparts, we can analyze the reasons for the observed reversal in selectivity.

We first note that both mutations disrupt the hydrogen bonding network at the active site between Tyr179, Asn241, and the backbone of Ala236. This generates a slightly larger cavity, which allows the substrate to move somewhat more than in the wild-type (Figure 5).

In the case of **TS-1-*R*^{Tyr179Ala}**, a hydrogen bond is formed between the imino group of the substrate and the backbone carbonyl of Ala236, an interaction that is neither present in the

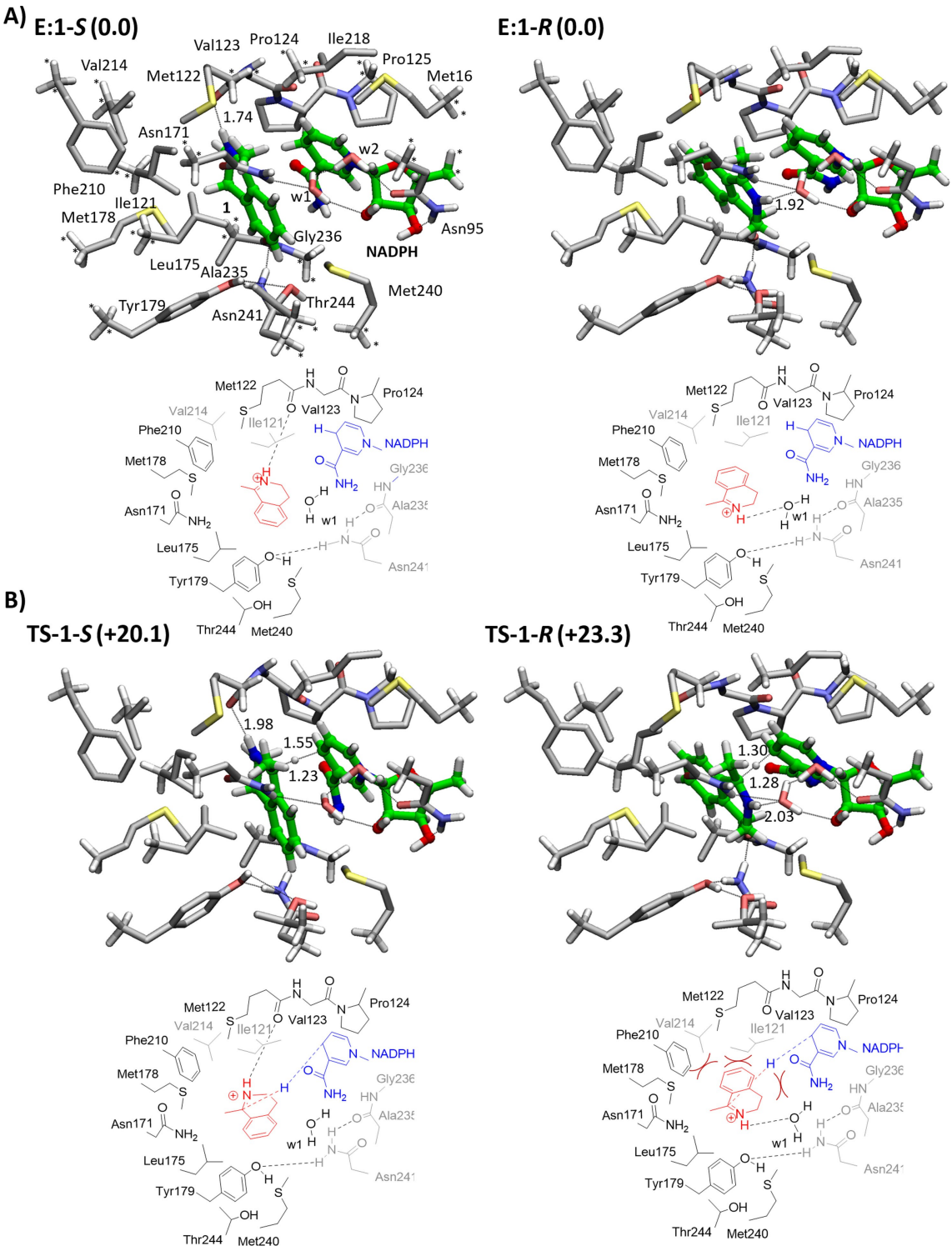

Figure 3. Optimized structures of A) the lowest-energy enzyme-substrate complexes **E:1-*S*** and **E:1-*R***, and B) lowest-energy transition states leading to the two enantiomers, **TS-1-*S*** and **TS-1-*R***. Selected distances are given in Å. Relative energies are indicated in kcal mol^{-1}. For clarity, most of the hydrogens are omitted. Atoms kept fixed during the optimizations are labeled with an asterisk.

TS-1-*S*^{Tyr179Ala} nor in the wild-type case. This is mainly caused by a slight rotation of the Asn241 and Met240 side chains, a movement that creates a small cavity that can accommodate the methyl substituent of the substrate.

This rationalization of the effect of Tyr179 on the enantioselectivity is different from the proposal in the literature, where this residue was suggested to form a hydrogen bond to the substrate and thereby orienting it in a specific way.[10] Such an interaction is observed in the crystal structure with the ***R*-2**

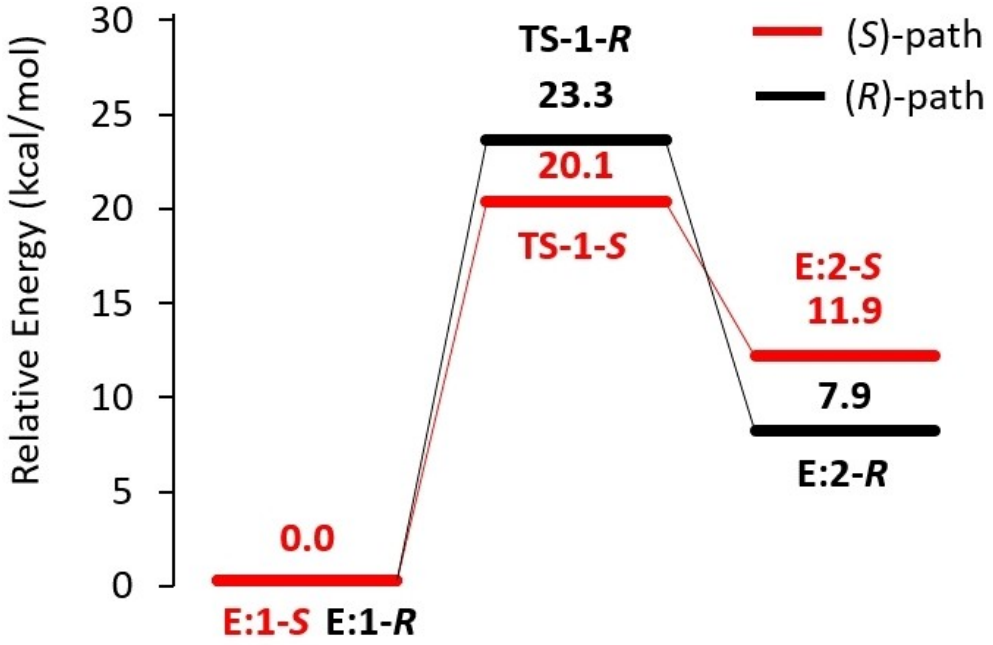

Figure 4. Calculated energy profiles for the reaction of substrate **1**.

product bound (see Figure 1). However, no hydrogen bond can be observed between the tyrosine and the substrate in the calculations, neither in the wild-type nor in the mutant.

In the case of **TS-1-*R*^{Asn241Ala}**, the orientation of the substrate in the active site is the same as in the wild-type case (**TS-1-*R***). Tyr179 is now slightly rotated to engage in a hydrogen bond with Thr244 (Figure 5). Importantly, the mutation of Asn241 and the rotation of Tyr179 create slightly more room for the substrate to move into that direction, alleviating the steric clashes with Val214 and Ile121. This therefore results in a lower energy for **TS-1-*R*^{Asn241Ala}** compared to **TS-1-*S*^{Asn241Ala}**.

The above analysis shows that it is not straightforward to predict the effects of a specific mutations on the enantioselectivity without calculations, because they can both cause the substrate to bind differently and also affect the interactions and energies of the transition states.

Finally, it is important to point out that we have, in the design of the active site model for the current calculations, used the crystal structure in complex with ***R*-2** (PDB 5FWN). The results for the wild-type active site are consistent with this enzyme being (*S*)-selective, as observed for the freshly purified enzyme. The fact that the calculations also reproduce the switch in enantioselectivity for the Tyr179Ala and Asn241Ala mutants lends further support to this notion. Nevertheless, it cannot be excluded that the enzyme somehow transforms to the (*R*)-selective form during the crystallization process.[10]

Reaction of 2-Propyl-piperideine

To further investigate the enantioselectivity of *Ao*IRED, we have considered the reaction with 2-propyl-piperideine, **3**, which shows the opposite selectivity compared to **1**, that is, >99% ee in favor of the *R*-product.[10] This substrate is smaller than **1** and has also an alkyl substituent with rotatable bonds, which will affect its binding to the active site and also the geometry of its transition states.

We have optimized 12 ES complexes with different substrate orientations and conformations. The lowest-energy *pro-R* and *pro-S* structures are shown in Figure 6, while the other structures are given in the Supporting Information.

In contrast to substrate **1**, the lowest-energy **E:3-*R*** and **E:3-*S*** binding modes differ by as much as 4.4 kcal mol^{-1}, in favor of the former (Figures 6 and 7).

In the **E:3-*S***, the imino group of the substrate forms hydrogen bond with carbonyl group of Met122, while in **E:3-*R*** the hydrogen bond is with the amide group of the cofactor. In both cases, the *n*-propyl substituent is located in the solvent-exposed side of catalytic pocket (Figure 6). The reason for the higher energy of **E:3-*S*** is that the *n*-propyl moiety clashes with Leu175, Tyr179 and Met240. Other *pro-S* binding modes that lack these clashes are higher in energy because of missing hydrogen bond of the imino group.

For each of the binding modes we have calculated the transition state for the hydride transfer. Interestingly, the lowest-energy TS leading to the *R*-product does not stem from the lowest-energy binding mode, but from an ES complex that is slightly higher in energy (**E:3-*R2***, +0.9 kcal/mol, see Supporting Information), and will therefore be called **TS-3-*R2***. The calculated barriers for **TS-3-*R2*** and **TS-3-*S*** are 20.6 kcal/mol and 21.1 kcal/mol, respectively. The lowest-energy enzyme-product complexes are +5.8 and +7.8 kcal/mol relative to **E:3-*R***, for the *S*- and *R*-pathways, respectively (see Supporting Information).

The computations are thus in agreement with the experimental outcome, favoring the formation of *R*-product,[10] but the calculated energy difference of 0.5 kcal/mol is underesti-

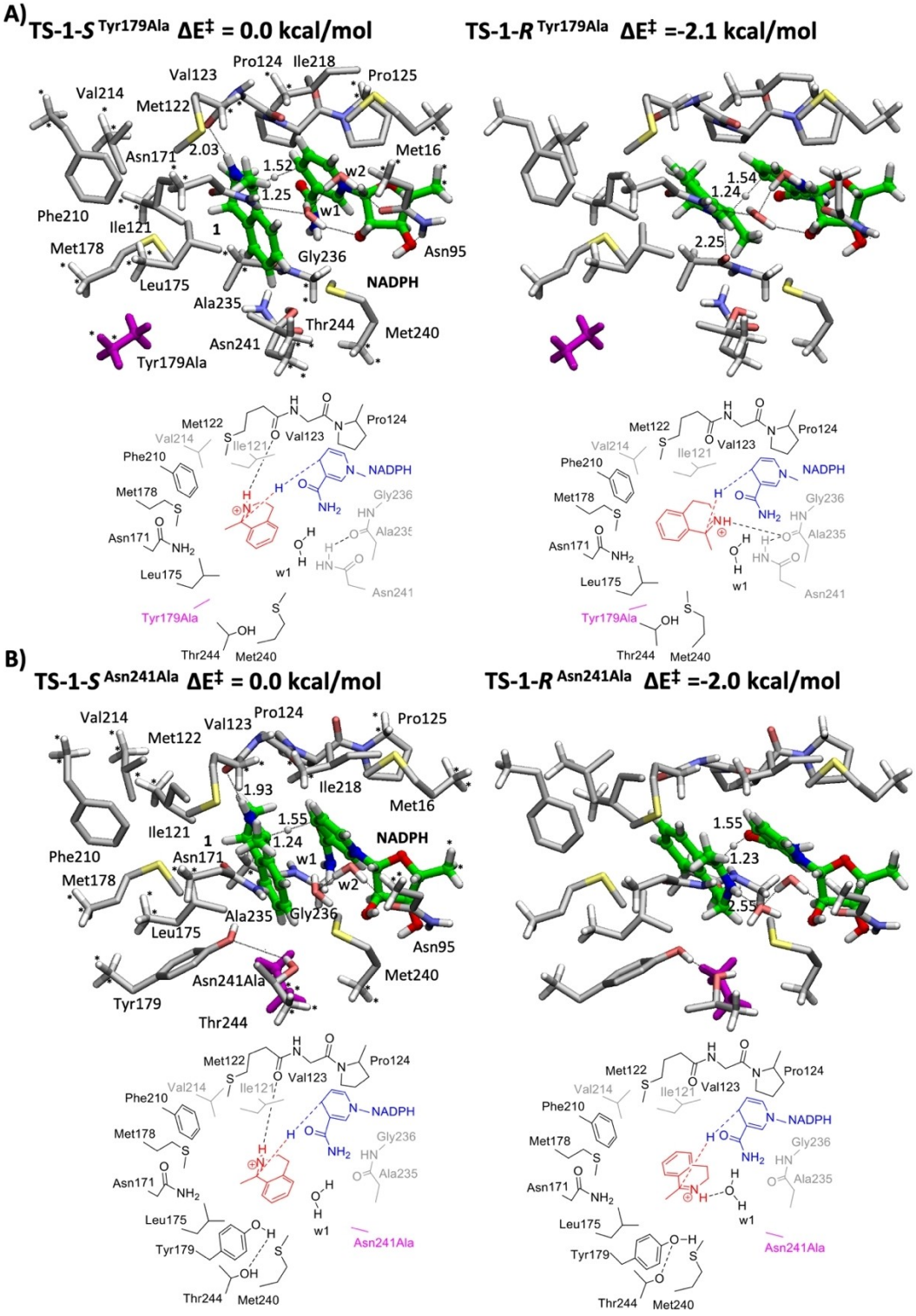

Figure 5. Optimized structures of the lowest-energy transitions states of A) Tyr179Ala (**TS-1-*S*^{Tyr179Ala}** and **TS-1-*R*^{Tyr179Ala}**) and B) Asn241Ala (**TS-1-*S*^{Asn241Ala}** and **TS-1-*R*^{Asn241Ala}**) mutations. Selected distances are given in Å. Relative energies for each pair of TSs are indicated in kcal mol^{-1}. For clarity, most of the hydrogens are omitted. Atoms kept fixed during the optimizations are labeled with an asterisk.

mated. As discussed in previous work on modeling enzymatic enantioselectivity, the reason for the underestimation is most likely related to the slight inflexibility of the active site model, which can miss to perfectly adapting to the size of the substrate.[13,14] However, it is important to underline that, since the modeling of enantioselectivity deals with very small energy differences, a perfect numerical agreement with experiments is very difficult to achieve, and the reproduction of experimentally

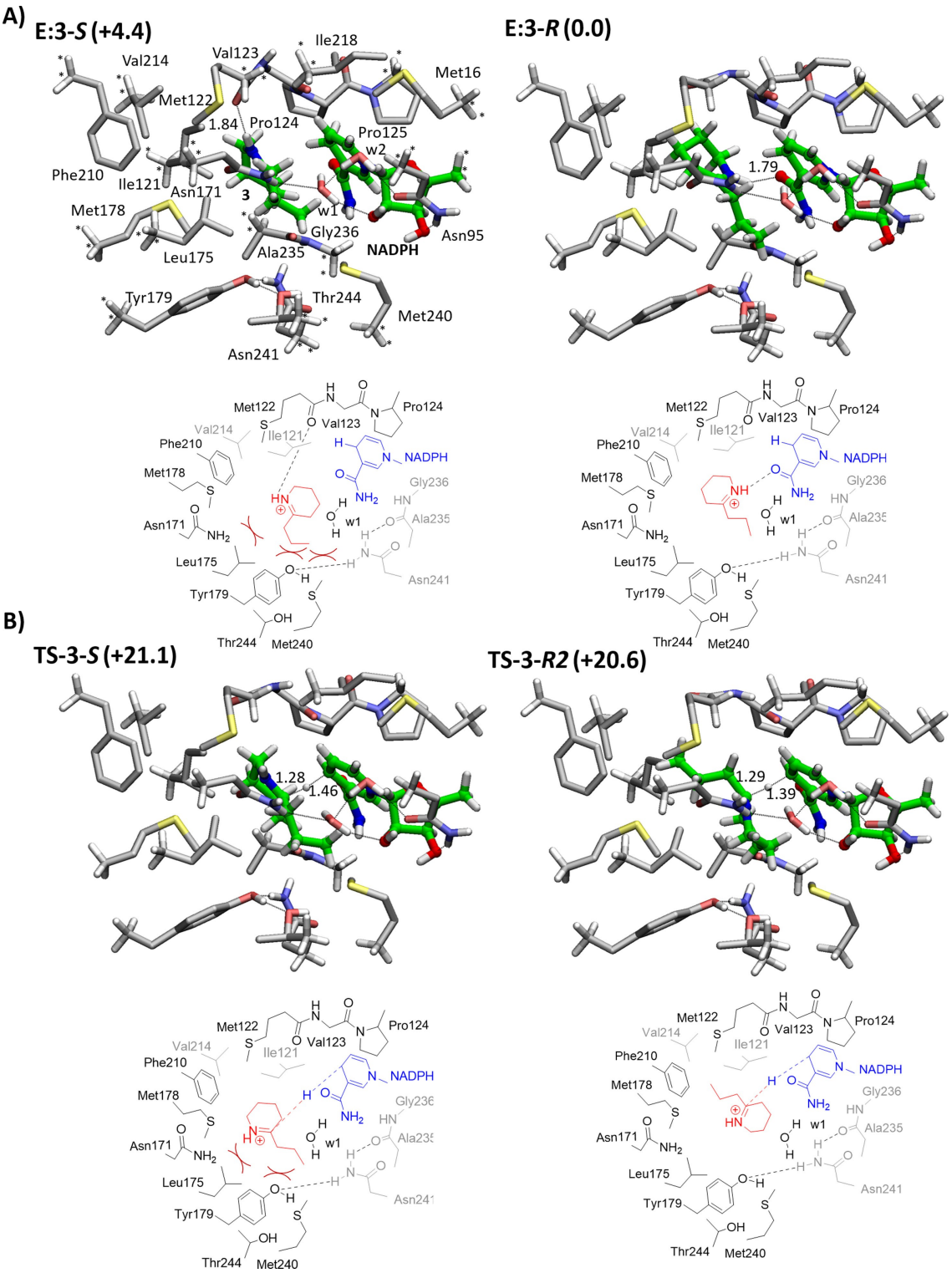

Figure 6. A) Optimized structures of the lowest-energy enzyme-substrate complexes **E:3-*S*** and **E:3-*R***, and B) lowest-energy transition states leading to the two enantiomers, **TS-3-*S*** and **TS-3-*R2***. Selected distances are given in Å. Relative energies are indicated in kcal mol^{-1}. For clarity, most of the hydrogens are omitted. Atoms kept fixed during the optimizations are labeled with an asterisk.

observed trends is generally considered as a very satisfactory result.

Comparisons of the optimized geometries of transitions states provide information about the origins of the observed enantioselectivity. Interestingly, the imino group is not involved in any hydrogen bonds in the lowest-energy transition states **TS-3-*R2*** and **TS-3-*S***. In **TS-3-*S***, the *n*-propyl group of the substrate clashes with the side chains of Tyr179 and Leu175. In

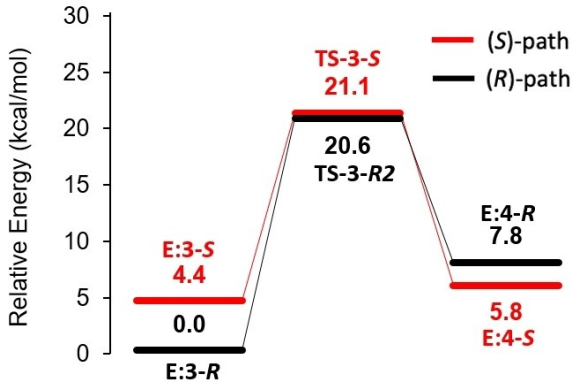

Figure 7. Calculated energy profiles for the reaction of substrate **3**.

TS-3-*R2* the *n*-propyl points in the opposite direction, making a better fit with the active site cavity.

An interesting aspect about substrate **3** is that there are other TSs for both the *R*- and the *S*-pathways that are not much higher in energy compared to **TS-3-*R2*** and **TS-3-*S*** (see Supporting Information). For example, there are three TSs in the *S*-pathway that are within 1 kcal mol^{-1} from **TS-3-*S***. This result shows that one has to consider all possible conformations and orientations of the substrate in the active site in order to reproduce and rationalize the enantioselectivity. It also shows that it is very difficult to *a priori* predict how a specific mutation will affect the relative energies, or what the consequences of even a small modification of the substrate will be on the enantioselectivity.

Conclusions

In the present study, we have investigated the reaction mechanism of imine reductase from *Amycolatopsis orientalis* using density functional theory calculations. This enzyme is of biocatalytic interest because it catalyzes the reduction of a broad range of cyclic imines to their corresponding amines, usually with high enantioselectivity.

The reactions of two substrates, 1-methyl-3,4-dihydroisoquinoline **1** and 2-propyl-piperideine **3**, have been investigated. A model of the active site consisting of over 300 atoms was built based on the recently solved X-ray structure of *Ao*IRED in complex with NAPDH and ***R*-2**, that is, the *R*-enantiomer of the product of the reaction with substrate **1**.[10] The calculated barriers are in agreement with available kinetic data. From a technical point of view, the calculations demonstrate that reactions starting from many enzyme-substrate complexes, with different substrate orientations and conformations, have to be taken into account in order to reproduce the experimental trends.

With help of a detailed analysis of the optimized geometries of the transition states, we could pinpoint the origins of the observed stereocontrol. Moreover, the effects of two mutations, Tyr179Ala and Asn241Ala, on the reaction of substrate **1** have been evaluated, whereby the calculations were also able to reproduce and rationalize the reversal of the stereochemical outcomes caused by these mutations.

Importantly for biocatalytic applications, it is argued that the full energy profiles for the reactions have to be considered, including the transition state energies, in order to understand the sources of the selectivity. It is not sufficient to compare the energies of the ES or EP complexes to predict the stereochemical outcome, because the factors causing energy differences in the ES or EP complexes might not be the same as those causing the differences in the transition states.

Supporting Information

Geometries and relative energies of different enzyme-substrate, enzyme-product, and transition state complexes; Superposition of lowest-energy enzyme-substrate complexes with the crystal structure; Results of non-covalent interaction analysis; Summary of calculated relative energies of different pathways; Absolute energies and energy corrections; Cartesian coordinates.

Acknowledgements

F. H. acknowledges financial support from the Swedish Research Council. M. P. thanks the Carl Tryggers Foundation for postdoctoral fellowship. X. S. thanks the Tianjin Synthetic Biotechnology Innovation Capacity Improvement Project (TSBICIP-CXRC-026) for financial support.

Conflict of Interest

The authors declare no conflict of interest.

Data Availability Statement

The data that support the findings of this study are available from the corresponding author upon reasonable request.

Keywords: biocatalysis · enantioselectivity · imine reductase · reaction mechanism · transition state

[1] J. H. Schrittwieser, S. Velikogne, W. Kroutil, *Adv. Synth. Catal.* **2015**, *357*, 1655.
[2] D. Ghislieri, N. J. Turner, *Top. Catal.* **2014**, *57*, 284.
[3] a) C. K. Savile, J. M. Janey, E. C. Mundorff, J. C. Moore, S. Tam, W. R. Jarvis, J. C. Colbeck, A. Krebber, F. J. Fleitz, J. Brands, P. N. Devine, G. W. Huisman, G. J. Hughes, *Science* **2010**, *329*, 305; b) E. Busto, V. Gotor-Fernandez, V. Gotor, *Chem. Rev.* **2011**, *111*, 3998; c) Q.-A. Chen, Z.-S. Ye, Y. Duan, Y. .-G. Zhou, *Chem. Soc. Rev.* **2013**, *42*, 497; d) G. Grogan, N. J. Turner, *Chem. Eur. J.* **2016**, *22*, 1900; e) H. J. Davis, T. R. Ward, *ACS Cent. Sci.* **2019**, *5*, 1120.
[4] a) T. Vaijayanthi, A. Chadha, *Tetrahedron: Asymmetry* **2008**, *19*, 93; b) M. Espinoza-Moraga, T. Petta, M. Vasquez-Vasquez, V. Felipe Laurie, L. A. B. Moraes, L. S. Santos, *Tetrahedron: Asymmetry* **2010**, *21*, 1988.

[5] a) K. Mitsukura, M. Suzuki, K. Tada, T. Yoshida, T. Nagasawa, *Org. Biomol. Chem.* **2010**, *8*, 4533; b) K. Mitsukura, M. Suzuki, S. Shinoda, T. Kuramoto, T. Yoshida, T. Nagasawa, *Biosci. Biotechnol. Biochem.* **2011**, *75*, 1778.
[6] a) M. Breuer, K. Ditrich, T. Habicher, B. Hauer, M. Keßeler, R. Stürmer, T. Zelinski, *Angew. Chem. Int. Ed.* **2004**, *43*, 788; b) T. C. Nugent, M. El-Shazly, *Adv. Synth. Catal.* **2010**, *352*, 753.
[7] T. Eguchi, Y. Oshiro, Y. Kuge, K. Mochida, T. Uwajima (Kyowa Hakko Kogyo Co., Ltd), US Patent Application 4929551, **1989**.
[8] W. De-Eknamkul, M. H. Zenk, *Phytochemistry* **1992**, *31*, 813.
[9] a) J. Zhu, H. Tan, L. Yang, L. Zhu, H. Ma, Z. Deng, Z. Tian, X. Qu, *ACS Catal.* **2017**, *7*, 7003; b) S. Velikogne, V. Resch, C. Dertnig, J. H. Schrittwieser, W. Kroutil, *ChemCatChem* **2018**, *10*, 3236; c) M. Sharma, J. Mangas-Sanchez, S. P. France, G. A. Aleku, S. L. Montgomery, J. I. Ramsden, N. J. Turner, G. A. Grogan, *ACS Catal.* **2018**, *8*, 12, 11534; d) M. D. Patil, G. Grogan, A. Bommarius, H. Yun, *ACS Catal.* **2018**, *8*, 12, 10985; e) P. Yao, Z. Xu, S. Yu, Q. Wu, D. Zhua, *Adv. Synth. Catal.* **2019**, *361*, 556; f) L. Yang, J. Zhu, C. Sun, Z. Deng, X. Qu, *Chem. Sci.* **2020**, *11*, 364; g) H. C. Büchsenschütz, V. Vidimce-Risteski, B. Eggbauer, S. Schmidt, C. K. Winkler, J. H. Schrittwieser, W. Kroutil, R. Kourist, *ChemCatChem* **2020**, *12*, 726; h) Z. Xu, P. Yao, X. Sheng, J. Li, J. Li, S. Yu, J. Feng, Q. Wu, D. Zhu, *ACS Catal.* **2020**, *10*, 8780.
[10] G. A. Aleku, H. Man, S. P. France, F. Leipold, S. Hussain, L. Toca-Gonzalez, R. Marchington, S. Hart, J. P. Turkenburg, G. Grogan, N. J. Turner, *ACS Catal.* **2016**, *6*, 3880.
[11] a) M. Rodriguez-Mata, A. Frank, E. Wells, F. Leipold, N. J. Turner, S. Hart, J. P. Turkenburg, G. Grogan, *ChemBioChem* **2013**, *14*, 1372; b) T. Huber, L. Schneider, A. Präg, S. Gerhardt, O. Einsle, M. Müller, *ChemCatChem* **2014**, *6*, 2248; c) H. Man, E. Wells, S. Hussain, F. Leipold, S. Hart, J. P. Turkenburg, N. J. Turner, G. Grogan, *ChemBioChem* **2015**, *16*, 1052; d) G. A. Aleku, S. P. France, H. Man, J. Mangas-Sanchez, S. L. Montgomery, M. Sharma, F. Leipold, S. Hussain, G. Grogan, N. J. Turner, *Nat. Chem.* **2017**, *9*, 961; e) M. Lenz, S. Fademrecht, M. Sharma, J. Pleiss, G. Grogan, B. M. Nestl, *Protein Eng. Des. Sel.* **2018**, *31*, 109; f) T. Meyer, N. Zumbrägel, C. Geerds, H. Gröger, H. H. Niemann, *Biomol. Eng.* **2020**, *10*, 1130.
[12] J. Guo, M. A. Higgins, P. Daniel-Ivad, K. S. Ryan, *J. Am. Chem. Soc.* **2019**, *141*, 12258.
[13] a) M. E. S. Lind, F. Himo, *Angew. Chem. Int. Ed.* **2013**, *52*, 4563; b) M. E. S. Lind, F. Himo, *ACS Catal.* **2014**, *4*, 415; c) M. E. S. Lind, F. Himo, *ACS Catal.* **2016**, *6*, 8145; d) S. Moa, F. Himo, *J. Inorg. Biochem.* **2017**, *175*, 259; e) X. Sheng, F. Himo, *ACS Catal.* **2017**, *7*, 1733; f) X. Sheng, F. Himo, *J. Am. Chem. Soc.* **2019**, *141*, 11230; g) M. Kazemi, X. Sheng, F. Himo, *Chem. Eur. J.* **2019**, *25*, 11945; h) F. Planas, M. J. McLeish, F. Himo, *ACS Catal.* **2019**, *9*, 5657; i) E. Jost, M. Kazemi, V. Mrkonjić, F. Himo, C. K. Winkler, W. Kroutil, *ACS Catal.* **2020**, *10*, 10500; j) X. Sheng, F. Himo, *ACS Catal.* **2020**, *10*, 13630.
[14] For a recent review, see: X. Sheng, M. Kazemi, F. Planas, F. Himo, *ACS Catal.* **2020**, *10*, 6430.
[15] Gaussian 16, Revision C.01, M. J. Frisch, G. W. Trucks, H. B. Schlegel, G. E. Scuseria, M. A. Robb, J. R. Cheeseman, G. Scalmani, V. Barone, G. A. Petersson, H. Nakatsuji, X. Li, M. Caricato, A. V. Marenich, J. Bloino, B. G. Janesko, R. Gomperts, B. Mennucci, H. P. Hratchian, J. V. Ortiz, A. F. Izmaylov, J. L. Sonnenberg, D. Williams-Young, F. Ding, F. Lipparini, F. Egidi, J. Goings, B. Peng, A. Petrone, T. Henderson, D. Ranasinghe, V. G. Zakrzewski, J. Gao, N. Rega, G. Zheng, W. Liang, M. Hada, M. Ehara, K. Toyota, R. Fukuda, J. Hasegawa, M. Ishida, T. Nakajima, Y. Honda, O. Kitao, H. Nakai, T. Vreven, K. Throssell, J. A. Montgomery, Jr., J. E. Peralta, F. Ogliaro, M. J. Bearpark, J. J. Heyd, E. N. Brothers, K. N. Kudin, V. N. Staroverov, T. A. Keith, R. Kobayashi, J. Normand, K. Raghavachari, A. P. Rendell, J. C. Burant, S. S. Iyengar, J. Tomasi, M. Cossi, J. M. Millam, M. Klene, C. Adamo, R. Cammi, J. W. Ochterski, R. L. Martin, K. Morokuma, O. Farkas, J. B. Foresman, D J. Fox, Gaussian, Inc., Wallingford CT, **2016**.
[16] a) C. Lee, W. Yang, R. G. Parr, *Phys. Rev. B: Condens. Matter Mater. Phys.* **1988**, *37*, 785; b) A. D. Becke, *J. Chem. Phys.* **1993**, *98*, 5648; c) S. Grimme, J. Antony, S. Ehrlich, H. A. Krieg, *J. Chem. Phys.* **2010**, *132*, 154104; d) S. Grimme, S. Ehrlich, L. Goerigk, *J. Comput. Chem.* **2011**, *32*, 1456.
[17] V. A. Marenich, C. J. Cramer, D. G. Truhlar, *J. Phys. Chem. B* **2009**, *113*, 6378.
[18] J. Contreras-Garcia, E. R. Johnson, S. Keinan, R. Chaudret, J.-P. Piquemal, D. N. Beratan, W. Yang, *J. Chem. Theory Comput.* **2011**, *7*, 625.

Manuscript received: November 2, 2021
Revised manuscript received: November 4, 2021